Diagonal control design for atomic force microscope piezoelectric tube nanopositioners

B. Bhikkaji, Y. K. Yong, I. A. Mahmood, and S. O. R. Moheimani

Citation: Rev. Sci. Instrum. **84**, 023705 (2013); doi: 10.1063/1.4790474
View online: http://dx.doi.org/10.1063/1.4790474
View Table of Contents: http://rsi.aip.org/resource/1/RSINAK/v84/i2
Published by the American Institute of Physics.

Related Articles

Damping of micromechanical structures by paramagnetic relaxation
Appl. Phys. Lett. 82, 3532 (2003)

Two-dimensional X pendulum vibration isolation table
Rev. Sci. Instrum. 70, 2150 (1999)

Additional information on Rev. Sci. Instrum.

Journal Homepage: http://rsi.aip.org
Journal Information: http://rsi.aip.org/about/about_the_journal
Top downloads: http://rsi.aip.org/features/most_downloaded
Information for Authors: http://rsi.aip.org/authors

ADVERTISEMENT

REVIEW OF SCIENTIFIC INSTRUMENTS **84**, 023705 (2013)

Diagonal control design for atomic force microscope piezoelectric tube nanopositioners

B. Bhikkaji,[1,a)] Y. K. Yong,[2,b)] I. A. Mahmood,[3,c)] and S. O. R. Moheimani[2,d)]
[1]*Indian Institute of Technology Madras, Chennai, India*
[2]*School of Electrical Engineering and Computer Science, The University of Newcastle, Callaghan, NSW 2308, Australia*
[3]*Department of Mechatronics Engineering, International Islamic University Malaysia, Malaysia*

(Received 31 May 2012; accepted 23 January 2013; published online 12 February 2013)

Atomic Force Microscopes (AFM) are used for generating surface topography of samples at micro to atomic resolutions. Many commercial AFMs use piezoelectric tube nanopositioners for scanning. Scanning rates of these microscopes are hampered by the presence of low frequency resonant modes. When inadvertently excited, these modes lead to high amplitude mechanical vibrations causing the loss of accuracy, while scanning, and eventually to break down of the tube. Feedback control has been used to damp these resonant modes. Thereby, enabling higher scanning rates. Here, a multivariable controller is designed to damp the first resonant mode along both the *x* and *y* axis. Exploiting the inherent symmetry in the piezoelectric tube, the multivariable control design problem is recast as independent single-input single-output (SISO) designs. This in conjunction with integral resonant control is used for damping the first resonant mode. © *2013 American Institute of Physics*. [http://dx.doi.org/10.1063/1.4790474]

I. INTRODUCTION

Atomic Force Microscopes (AFMs) were first designed during 1980s,[1] for tracing out the topography of material surfaces at micro to atomic resolution. Since then AFMs have been used extensively in various scientific fields such as high-speed, real-time imaging of biological cells,[2–5] nanomachining and fabrication,[6–9] surface nano-lithography,[10–12] and nano-metrology.[13,14] The reason for this versatility being the fact that they can be adapted to most experimental surroundings such as ambient air, liquids, gases, high temperatures, low temperatures, vacuum, etc.

The main impediment when using AFMs are the slow scanning speeds. Slow scans though very accurate leads to long waiting periods (before getting an image of the surface topography).[15] Fast scans are largely inaccurate and do not produce repeatable results. This is largely due to the mechanical vibrations set off by the resonant modes of the scanner. In situations where material samples have short half life, fast scanning becomes necessary. In standard commercial AFMs, this problem can be alleviated by compensating for the mechanical vibrations by designing feedback controllers. This paper presents a multivariable feedback control scheme that is very effective and at the same time simple to use for practitioners of atomic force microscopy. The control scheme was implemented on a piezoelectric tube scanner. The proposed control scheme can also be implemented on flexure-based nanopositioners, which have symmetrical properties.[16]

The scanning unit of an AFM has a cantilever with a sharp probe (of few atomic dimensions in width). The sample, for which a topographical map is desired, is placed such that the probe touches the surface of the sample. A laser source is focused on the probe end of the cantilever, and the reflection from the cantilever is captured by a position sensitive photodiode (PSD), see Fig. 1. The sample surface is scanned by moving it (the sample) in a raster pattern, causing the cantilever to deflect due to variations in the sample topography. These deflections are measured by the laser and the PSD, which, in turn, is used for generating the topography of the surface.

When actuating the piezoelectric tube in a raster pattern, the tube tracks a triangular waveform along the *x*-axis and a slowly increasing ramp, or a slowly increasing staircase function, along the *y*-axis. The fundamental frequency of the triangular waveform is referred to as the scanning rate. Actuation of piezoelectric tubes are hampered by the presence of low mechanical resonance frequencies. Higher scanning rates excite the resonance, inducing mechanical vibrations. Typically, to avoid vibrations, the scanning rates are restricted to 1% of the resonance frequency.[17–19]

A standard paradigm for the actuation of a piezoelectric tube has been to design a feedback controller that would damp the resonance along the *x* axis,.[20–24] This would enable the tube to track triangular waveforms with higher fundamental frequencies than 1% of the resonance frequency (or achieve higher scanning rates). As the tracking signal along the *y* axis is either a slowly varying ramp, or a staircase function, the actuation along the *y* axis is done in open loop, which is similar to the feedback configuration shown in Fig. 5. However, this would not completely eliminate vibrations due to cross coupling between the *x* and *y* axis. Dynamics-coupling between the piezoelectric tube scanner axes causes significant positioning errors[25–27] that distorts AFM images.[28] A more comprehensive paradigm would be to design a multivariable controller that would damp resonances of all the

a)Electronic mail: bharath.bhikkaji@iitm.ac.in.
b)Electronic mail: yuenkuan.yong@newcastle.edu.au.
c)Electronic mail: am.iskandar@iium.edu.my.
d)Corresponding author. Electronic mail: reza.moheimani@newcastle.edu.au.

 © 2013 American Institute of Physics

FIG. 1. Schematic of an AFM.

transfer-functions involved, see Fig. 6. Though multivariable control designs have been attempted before, the design methodologies have assumed the dynamics along the x and y axis to be independent;[29–33] thereby, ignoring the cross coupling. Cross coupling makes designing multivariable controllers a tedious task; in most cases, leading to the minimization of non-covex cost functions.[34] This paper presents an elegant method for designing a multivariable controller for piezoelectric tubes in the presence of cross coupling. In particular, an IRC controller will be designed for damping the resonances.

II. PIEZOELECTRIC TUBE

The piezoelectric tube scanner considered here is a thin walled cylindrical tube made of piezoelectric material. The inner and outer walls of the tube are coated with a layer of silver. The silver coats act as electrodes enabling actuation through electrical signals. The outer electrode is divided into two continuous cylindrical sections $x - y$ and z. The lower $x - y$ electrode being much larger in dimension than the upper z electrode. The $x - y$ section is further split into four equal parts $x +$, $y +$, $x -$, and $y -$, see Fig. 2 for an illustration.

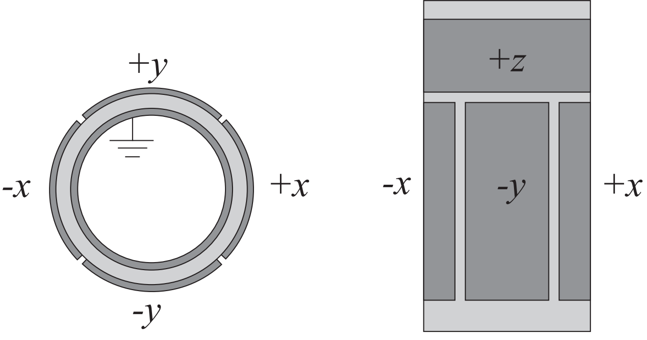

FIG. 2. Schematics of the piezoelectric tube scanner.

In an AFM, the $x - y$ end of the tube is fixed to the base, while the z end is glued to an aluminum cube. The aluminum cube serves as a stage for placing the sample. The inner electrode of the tube is earthed all times, while the outer electrodes are biased with electrical signals for actuation. Typically, $x +$ and $y +$ are the actuation points, while $x -$ and $y -$ denote the sensing points. When voltage signals $\mathrm{v}_{\mathrm{x}+}$ and $\mathrm{v}_{\mathrm{y}+}$ are applied at $x +$ and $y +$, respectively, the piezoelectric tube deforms inducing voltages $\mathrm{v}_{\mathrm{x}-}$ and $\mathrm{v}_{\mathrm{y}-}$ at $x -$ and $y -$, respectively, due to piezoelectric effect.

III. EXPERIMENTAL SETUP

An NT-MDT NTEGRA scanning probe microscope (SPM) is used for performing experiments. This SPM is capable of performing scans in air and liquid. The SPM software limits the image resolution relative to scanning speed. At the highest resolution, 256 × 256 scan lines, the fastest achievable scanning frequency is limited to 31 Hz. The SPM is configured to operate as an AFM. The piezoelectric tube scanner of the SPM is replaced by the above mentioned tube scanner. The $x +$ and $y +$ axes of the tube are driven by a NANONIS bipolar high voltage amplifier HVA4. This amplifier has a maximum gain of 40 and a voltage range of 400 V. Two ADE Technologies 8810 capacitive sensors were placed in close proximity to the adjacent surfaces of the sample holder (aluminum cube) to observe the displacements of the tube along the x and y axes; see Fig. 1. The AFM controller was used to generate the $x +$ and $y +$ signals. These were accessed through the AFM signal access module and were applied to the controlled piezoelectric tube scanner through the high voltage amplifiers. A dSPACE-1103 rapid prototyping system was used to implement the x and y axes feedback controllers in real-time. The z-axis displacement was controlled using the AFM software and circuitry.

The nanopositioning system is interpreted as having two linear subsystems

$$Y_{\mathrm{v}}(s) = G_{\mathrm{v}}(s)U(s) \tag{1}$$

and

$$Y_{\mathrm{d}}(s) = G_{\mathrm{d}}(s)U(s), \tag{2}$$

where $Y_{\mathrm{v}}(s)$ is the Laplace transform of $[\mathrm{v}_{\mathrm{x}-}, \mathrm{v}_{\mathrm{y}-}]^{\top}$, voltages induced at the sensing patches $x -$ and $y -$, $Y_{\mathrm{d}}(s)$ is the Laplace transform of $[\mathrm{d}_{\mathrm{x}}, \mathrm{d}_{\mathrm{y}}]^{\top}$, displacement measurements of the capacitive sensors along x and y directions, $U(s)$ is the Laplace transform of $[\mathrm{v}_{\mathrm{x}+}, \mathrm{v}_{\mathrm{y}+}]^{\top}$, voltage signals applied at the $x +$ and $y +$ electrodes,

$$G_{\mathrm{v}}(s) = \begin{bmatrix} G_{xx}(s) & G_{xy}(s) \\ G_{yx}(s) & G_{yy}(s) \end{bmatrix} \tag{3}$$

and

$$G_{\mathrm{d}}(s) = \begin{bmatrix} G_{\mathrm{d_x x}}(s) & G_{\mathrm{d_x y}}(s) \\ G_{\mathrm{d_y x}}(s) & G_{\mathrm{d_y y}}(s) \end{bmatrix}, \tag{4}$$

transfer-functions relating the inputs $[\mathrm{v}_{\mathrm{x}+}, \mathrm{v}_{\mathrm{y}+}]^{\top}$ and the outputs $[\mathrm{v}_{\mathrm{x}-}, \mathrm{v}_{\mathrm{y}-}]^{\top}$ and $[\mathrm{d}_{\mathrm{x}}, \mathrm{d}_{\mathrm{y}}]^{\top}$, respectively.

Due to symmetry, the dynamic response of piezoelectric tubes to inputs along x and y axis will be similar. That is, in the

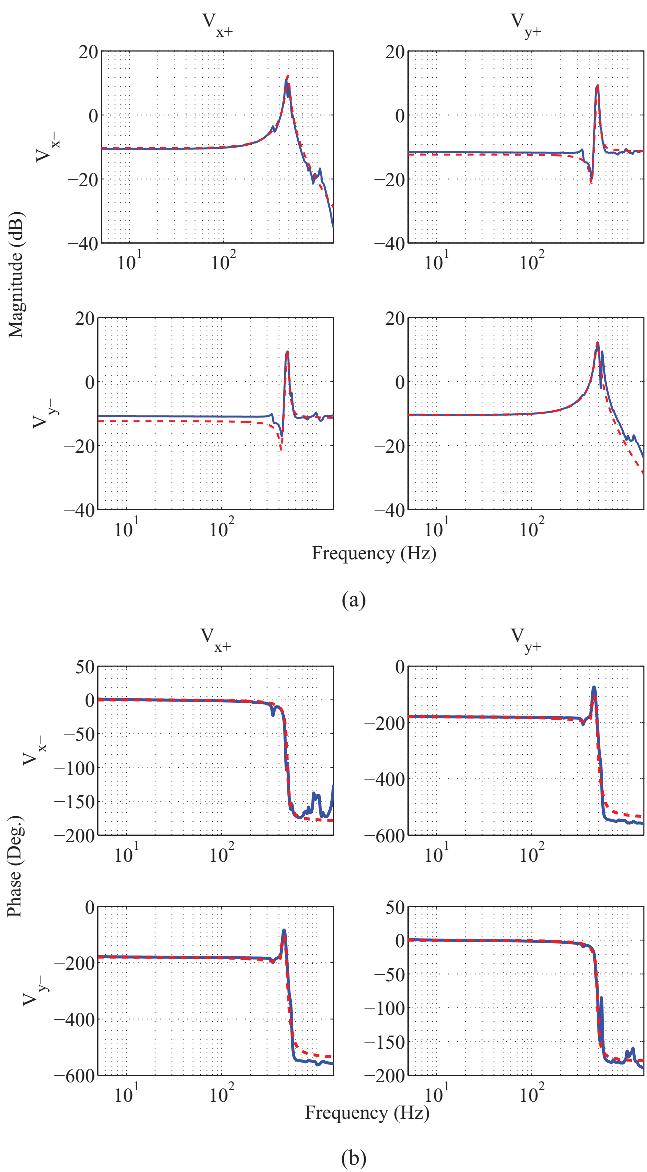

FIG. 3. (a) Magnitude and (b) phase of the frequency response functions (FRFs) relating the inputs $[v_{x+}, v_{y+}]^{\top}$ and the outputs $[v_{x-}, v_{y-}]^{\top}$. Dashed plots (– –) denote the magnitude response of the models estimated, while the continuous (–) plots denote the experimentally determined magnitude response.

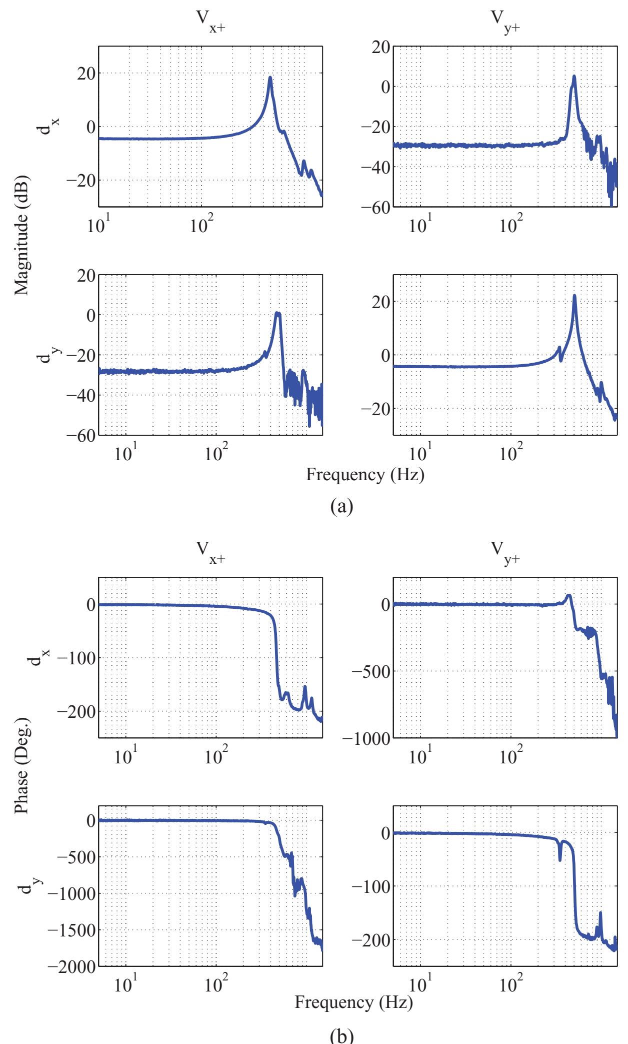

FIG. 4. (a) Magnitude and (b) phase of the frequency response functions (FRFs) relating the inputs $[v_{x+}, v_{y+}]^{\top}$ and the capacitive sensor outputs $[d_x, d_y]^{\top}$.

case of the voltage subsystem $G_v(s)$, it is expected that $G_{xx}(s) = G_{yy}(s)$ and $G_{xy}(s) = G_{yx}(s)$, while in the case of the $G_d(s)$, it is expected that $G_{d_x x}(s) = G_{d_y y}(s)$ and $G_{d_x y}(s) = G_{d_y x}(s)$. It will be later shown that this property allows for the decoupling of the tube dynamics and consequently enabling the conversion of the multivariable design problem to a simpler SISO design problem without having to neglect the cross coupling.

IV. SYSTEM IDENTIFICATION

Swept sine waves v_{x+} and v_{y+}, within the frequency range of 10 Hz to 1.6 kHz, are applied at the $x+$ and $y+$ electrodes, respectively. The corresponding voltages v_{x-} and v_{y-} induced at $x-$ and $y-$ electrodes are recorded. The frequency response functions (FRF) relating the inputs $[v_{x+}, v_{y+}]^{\top}$ and the recorded outputs $[v_{x-}, v_{y-}]^{\top}$ are plotted in Figs. 3(a) and 3(b). The displacements d_x and d_y measured by the capacitive sensors are also recorded and the FRFs relating them to the input $[v_{x+}, v_{y+}]^{\top}$ are plotted in Figs. 4(a) and 4(b).

Here, subsystem (1) will be used for control design while the capacitive sensor responses, i.e., subsystem (2), will be used for monitoring the displacements along x and y axes. Therefore, only transfer-functions of the matrix $G_v(s)$, (1), are modeled.

Due to the symmetry, we expect $G_{xx}(j\omega) = G_{yy}(j\omega)$ and $G_{xy}(j\omega) = G_{yx}(j\omega)$. However, invariably due to errors introduced when manufacturing a tube (such as the tube being not uniformly thick or not having a constant density), unsymmetrical gluing of the aluminum cube and uneven fastening of to the tube to the base, they can be only approximately equal. This is evident from Fig. 3. Nevertheless, for control design, it is assumed that $G_{xx}(j\omega) = G_{yy}(j\omega)$ and $G_{xy}(j\omega) = G_{yx}(j\omega)$.

The following models have been fitted to the FRF data plotted in Fig. 3,

$$G_1(s) = \frac{2.851e006}{s^2 + 225s + 9.432e006} \tag{5}$$

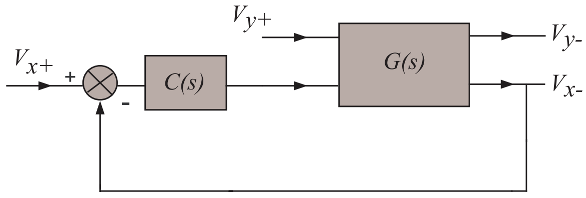

FIG. 5. Standard control paradigm followed for the actuation of piezoelectric tubes.

and

$$G_2(s) = \frac{-0.27(s^2 + 160s + 7.2e06)}{(s^2 + 225s + 9.432e06)} \times \frac{(s^2 - 600s + 1.1e07)}{(s^2 + 225s + 9.432e06)}, \tag{6}$$

where $G_1(s) = G_{xx}(s) = G_{yy}(s)$ and $G_2(s) = G_{xy}(s) = G_{yx}(s)$.

V. CONTROL METHODOLOGY

The standard paradigm for the control of piezoelectric tubes has been implemented to damp the resonance along the x axis. That is, to damp the resonance of $G_{xx}(s)$, using a feedback controller, and to actuate the tube in a raster pattern, see Fig. 5. This, however, does not completely eliminate vibrations, as the resonance along the y axis is not damped.

In order to damp resonances along both axes, a multivariable controller, Fig. 6, that regulates both inputs have to be designed. In Refs. 29, 30, and 35, the authors have ignored cross coupling, i.e., have set $G_{xy}(s) = G_{yx}(s) = 0$ in (3), and designed controllers of the form

$$C(s) = \begin{bmatrix} C_{xx}(s) & 0 \\ 0 & C_{yy}(s) \end{bmatrix} \tag{7}$$

to damp resonances along both the axes. This could result in closed-loop instabilities. For example, it can be checked that,

$$C_{xx}(s) = C_{yy}(s) = \frac{-10000}{s + 5000} \tag{8}$$

will stabilize $G_v(s)$, (3), when $G_1(s) = G_{xx}(s) = G_{yy}(s)$, and $G_{xy}(s) = G_{yx}(s) = 0$. But, it will not stabilize $G_v(s)$ with $G_{xy}(s) = G_{yx}(s) = G_2(s)$.

To the best of authors' knowledge, fully multivariable controllers of the form

$$C(s) = \begin{bmatrix} C_{xx}(s) & C_{xy}(s) \\ C_{yx}(s) & C_{yy}(s) \end{bmatrix} \tag{9}$$

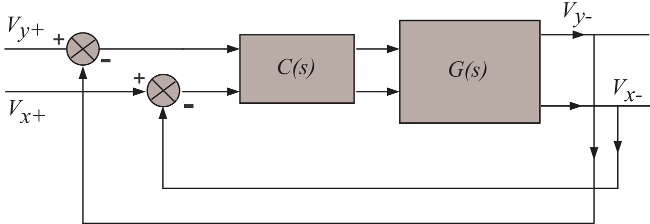

FIG. 6. Multivariable control of the piezoelectric tube.

are rarely designed for piezoelectric tube scanners. Note that

$$\begin{aligned} G_v(s) &= \begin{bmatrix} G_{xx}(s) & G_{xy}(s) \\ G_{yx}(s) & G_{yy}(s) \end{bmatrix} \\ &= \begin{bmatrix} G_1(s) & G_2(s) \\ G_2(s) & G_1(s) \end{bmatrix} \\ &= M^\top \begin{bmatrix} G_+(s) & 0 \\ 0 & G_-(s) \end{bmatrix} M, \end{aligned} \tag{10}$$

where

$$M = M^\top = \frac{1}{\sqrt{2}} \begin{bmatrix} 1 & 1 \\ 1 & -1 \end{bmatrix}, \tag{11}$$

$$G_+(s) = G_1(s) + G_2(s), \tag{12}$$

and

$$G_-(s) = G_1(s) - G_2(s). \tag{13}$$

Similarly, in C(s), (9), if $C_1(s) = C_{xx}(s) = C_{yy}(s)$ and $C_2(s) = C_{xy}(s) = C_{yx}(s)$ then

$$C(s) = M^\top \begin{bmatrix} C_+(s) & 0 \\ 0 & C_-(s) \end{bmatrix} M, \tag{14}$$

where

$$C_+(s) = C_1(s) + C_2(s) \tag{15}$$

and

$$C_-(s) = C_1(s) - C_2(s). \tag{16}$$

This implies that Loop transfer-function of Fig. 6 is

$$\begin{aligned} L(s) &= G_v(s)C(s) \\ &= M^\top \begin{bmatrix} C_+(s)G_+(s) & 0 \\ 0 & C_-(s)G_-(s) \end{bmatrix} M. \end{aligned} \tag{17}$$

Hence, the closed loop poles are zeros of

$$\begin{aligned} &\mathrm{I} + L(s) = \mathrm{I} + G_v(s)C(s) \\ &= M^\top \begin{bmatrix} 1 + C_+(s)G_+(s) & 0 \\ 0 & 1 + C_-(s)G_-(s) \end{bmatrix} M, \end{aligned} \tag{18}$$

where I is the 2×2 identity matrix. This in turn implies that the closed loop poles are zeros of

$$1 + C_+(s)G_+(s) = 0 \tag{19}$$

and

$$1 + C_-(s)G_-(s) = 0. \tag{20}$$

Thus, designing a multivariable controller now boils down to designing controllers $C_+(s)$ and $C_-(s)$ for scalar transfer-functions $G_+(s)$ and $G_-(s)$, respectively. Designing controllers for SISO plants are mathematically tractable and their stability properties can be easily analyzed using root-locus plots. Here, integral resonant control (IRC), described in Ref. 36, is used for designing controllers $C_+(s)$ and $C_-(s)$, as they are known to give good performance and posses a simple model structure.

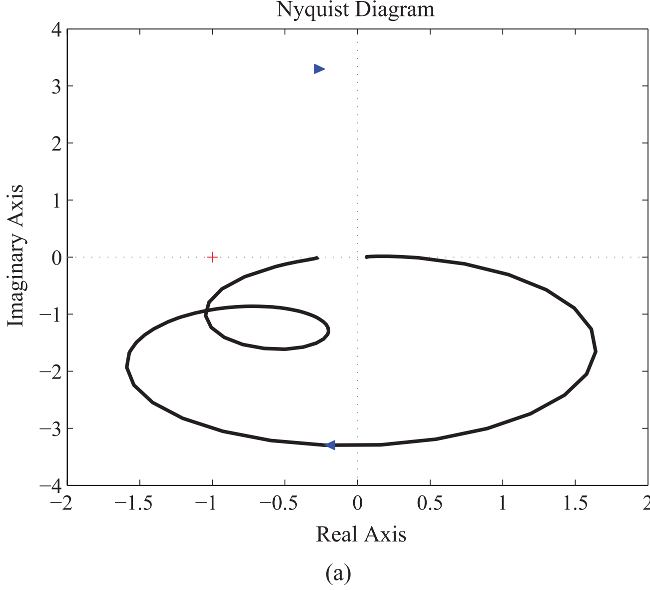

(a)

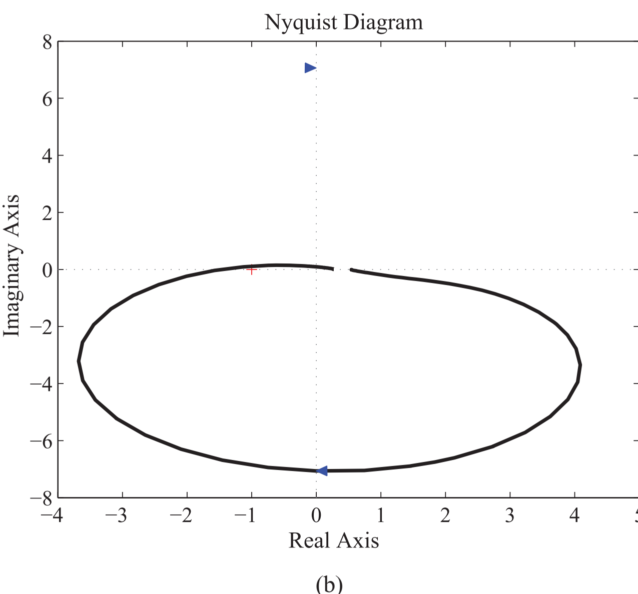

(b)

FIG. 7. Nyquist plot of (Top) $G_+(s)$ for $\omega > 0$, and (Bottom) $G_-(s)$ for $\omega > 0$.

It is worth noting that, when a square matrix of transfer-functions G, is diagonalized $G(s) = C^{-1}(s)\Sigma C(s)$, the companion matrix $C(s)$ is a function of the Laplace variable s. Even if $G(s)$ is symmetric. However, an exception to this rule is the case mentioned above, when $G(s)$ is 2×2 and the diagonal elements being equal.

VI. EXPERIMENTAL RESULTS

A SISO IRC controller has the following model structure:

$$C(s) = \frac{K}{s + Kd}, \tag{21}$$

where K and d are strictly positive numbers. It can be checked that an IRC controller is negative imaginary, that is the imaginary part of $C(i\omega)$ (Imag($C(i\omega)$)) is strictly negative for all $\omega > 0$. In Ref. 37, it has been shown that for transfer-functions

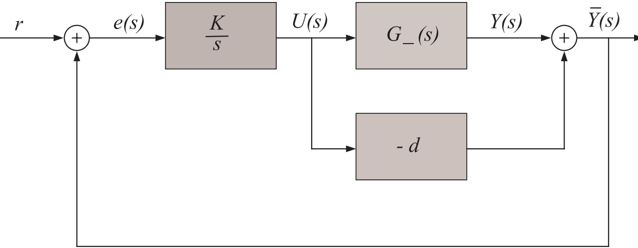

FIG. 8. Closed-loop system with controller $C(s)$ around $\bar{G}_- = G_-(s) - d$.

$G(s)$ and $C(s)$ that are strictly negative imaginary the closed loop system, in positive feedback configuration, is internally stable if

1. $L(\infty) = G(\infty)C(\infty) = 0$,
2. $|G(0)C(0)| < 1$.

In other words, if $G_+(s)$ and $G_-(s)$ are negative imaginary then stabilizing IRC controllers could be designed for each of them. In Figs. 7(a) and 7(b), Nyquist plots of $G_+(s)$ and $G_-(s)$, respectively, are plotted. As $G_+(i\omega)$ lies completely in the lower half plane for all $\omega > 0$ it is negative imaginary. While $G_-(s)$ has a small portion that has a positive imaginary part. Considering the deviation of $G_-(s)$ from being negative imaginary as insignificant, IRC controllers are designed using the above result.

Note that by construction $C(\infty) = 0$. Therefore, $L_-(\infty) = G_-(\infty)C(\infty) = 0$. Since

$$C(0) = \frac{1}{d}, \tag{22}$$

the second condition implies

$$|d| > G_-(0). \tag{23}$$

It can be checked that $G_-(0) = 0.5426$. Hence, $|d| > 0.5426$. In the following, the root-locus procedure presented in Ref. 36 for designing the IRC is outlined. Consider the control schematic shown in Fig. 8. Note from Fig. 8 that the input

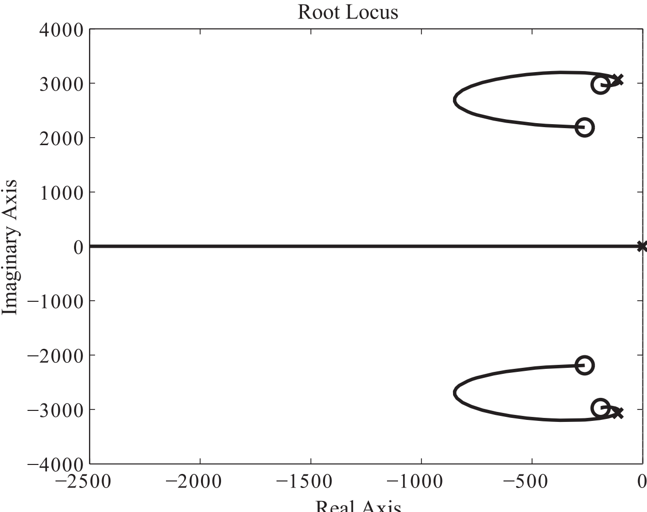

FIG. 9. Root locus plot of $\frac{-K(G_-(s)-d)}{s}$ with $K > 0$.

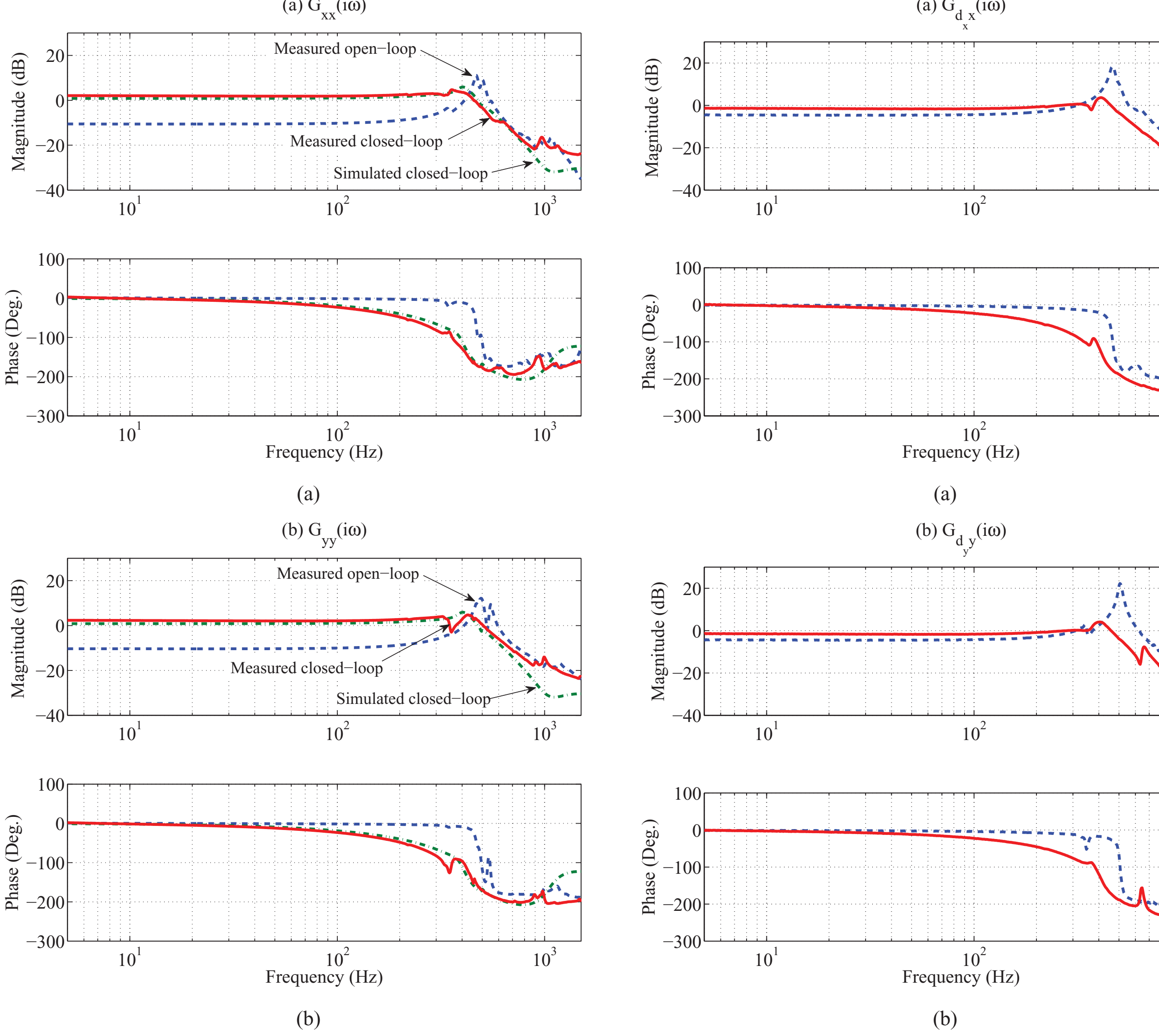

FIG. 10. Magnitude and phase responses of the open and closed loop FRFs relating (a) input v_{x+} and output v_{x-}, and (b) input v_{y+} and output v_{y-}. Dashed-dotted plots (-.) denote simulated closed loop FRFs, dashed plots (–) denote open loop FRFs, and continuous plots (–) denote experimentally determined closed loop FRFs.

FIG. 11. Magnitude and phase responses of the closed loop FRFs relating (a) input v_{x+} and output d_x, and (b) input v_{y+} and output d_y. Dashed plots (- -) denote open loop FRFs and continuous plots (–) denote experimentally determined closed loop FRFs.

to the plant is given by

$$\begin{aligned} U(s) &= \frac{K}{s}(\bar{Y}(s) + r(s)) \\ &= \frac{K}{s}(Y(s) - dU(s) + r(s)), \end{aligned} \tag{24}$$

which implies

$$U(s) = \frac{\frac{K}{s}}{1 + d\frac{K}{s}}(Y(s) + r(s)). \tag{25}$$

Therefore,

$$\begin{aligned} Y(s) &= G_-(s)U(s) \\ &= G_-(s)\frac{\frac{K}{s}}{1 + d\frac{K}{s}}(Y(s) + r(s)), \\ &= G_-(s)C_-(s)(Y(s) + r(s)), \end{aligned} \tag{26}$$

where

$$\begin{aligned} C_-(s) &= \frac{\frac{K}{s}}{1 + d\frac{K}{s}} \\ &= \frac{K}{s + Kd} \end{aligned} \tag{27}$$

is the IRC controllers. Furthermore, (26) leads to

$$Y(s) = \frac{G_-(s)C_-(s)}{1 - G_-(s)C_-(s)}r(s). \tag{28}$$

In words, designing an IRC amounts to subtracting a d from $G_-(s)$ and wrapping an integral controller around $G_-(s) - d$ in positive feedback. Here, d is set to 0.8 and K is chosen to be 10^4, using the root locus of $\frac{-K(G_- - d)}{s}$ obtained by varying K, see Fig. 9, so that sufficient damping is imparted. Using the

Open-loop images

5Hz 10Hz 15.6Hz 31.25Hz

3D view

FIG. 12. Open-loop images (256×256 scan lines) of a 4 μm × 4 μm scan area.

values of K and d, the IRC controller for $G_{-}(s)$ is given by

$$C_{-}(s) = \frac{10^4}{s + 8000}. \tag{29}$$

Similarly, it can be shown that the same values of K and d would render the $G_{+}(s)$ stable in positive feedback, more explicitly the IRC controller $C_{+}(s)$ for $G_{+}(s)$ can be chosen to be equal to $C_{-}(s)$.

In Figs. 10(a) and 10(b), open loop data are plotted along with the simulated closed loop model for $G_{xx}(s)$ and $G_{yy}(s)$. Simulations predict a 20 dB damping. As done in Sec. IV, swept sine waves, within the frequency range of 10 Hz to 1.6 kHz, are applied at the $x+$ and $y+$ electrodes, and the corresponding voltages induced at the $x-$ and $y-$ electrodes are measured in closed loop. The closed loop FRFs relating the inputs applied at $x+$ and $y+$ electrodes and outputs recorded at $x-$ and $y-$ electrodes are plotted in Figs. 10(a) and 10(b). It can be observed from the plots that simulations closely match the experimental results. A similar damping can be observed in the closed loop FRFs relating the inputs and the capacitive sensor outputs plotted in Figs. 11(a) and 11(b).

It had been noted that,[20] the damping at the resonant modes increase, while the system gains drop a little with increasing sample mass (i.e., mass of the samples placed on the scanner). This would not alter the negative imaginary property, and furthermore the reduction in gains will not undermine the stability, as the stability conditions, Eq. (23), will not be violated for both $G_{+}(0)$ and $G_{-}(0)$.

VII. AFM IMAGES

In this section, scan images of a calibration grating are obtained to evaluate the performance of the damping controller. A MikroMasch TZG2 calibration grating which has parallel rectangular features, with 3 μm period and 108 nm height, was used during the experiments. A contact mode cantilever with a resonance frequency of 13 kHz was used to perform scans. The first dominant mode of the x and y axes was suppressed in closed-loop using the integral resonant control technique presented in Sec. V. Open- and closed-loop images of a 4 μm×4 μm area of the grating were obtained in constant height contact mode at 5 Hz, 10 Hz, 15.6 Hz, and 31.25 Hz. The pixel resolution of these images is 256 × 256.

Figs. 12 and 13 illustrate the open- and closed-loop images (with activated IRC), respectively. Oscillations are visible in all open-loop scans, which distort the images severely,

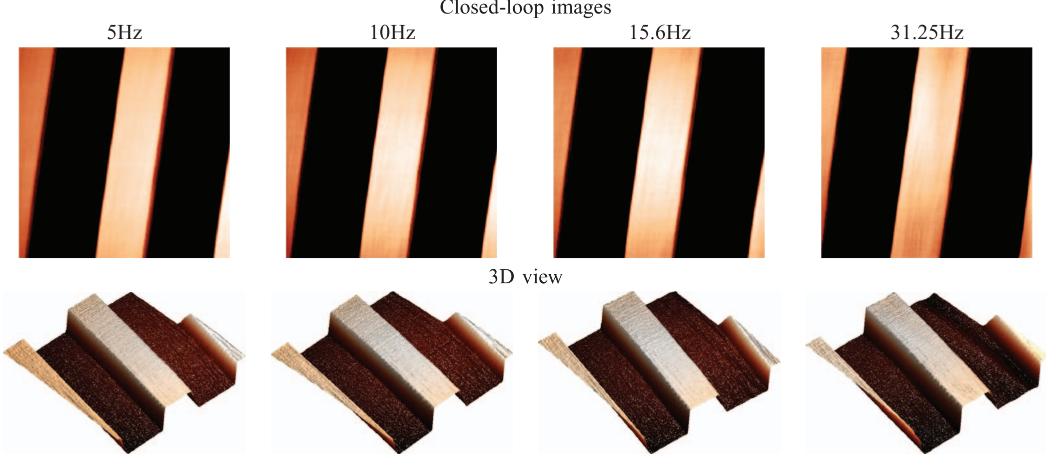

FIG. 13. Closed-loop images (256×256 scan lines) of a 4 μm × 4 μm scan area.

in particular, at 31.25 Hz. Oscillations are also observed in time signals. With the IRC activated, oscillations are eliminated in all four scan frequencies.

VIII. CONCLUSION

Atomic force microscopes use piezoelectric tubes for nanopositioning. Piezoelectric tubes possess lightly damped resonant modes that cause mechanical vibrations. Thereby, restricting the scanning rates to less than 1% of the first resonance frequency. In this paper, a symmetrically quartered piezoelectric tube, typically used in AFMs as nanopositioner, was considered. In order to actuate this tube in a raster pattern, resonant modes along both x and y axes have to be damped. It was noted control designs that neglect the cross coupling in the tube dynamics could cause closed loop instability. As the tube is symmetrically quartered, the transfer-function matrix relating the voltages applied at the $x+$ and $y+$ electrodes and the voltages induced at the $x-$ and $y-$ electrodes is symmetric. A controller with a similar structure as the plant was found to convert the multiple-input multiple-output (MIMO) control design problem into independent SISO designs. IRC controllers were designed for the individual SISO plants. A 20 dB damping was achieved along both the x and y axes. Scan images were recorded in open- and closed-loop at 5 Hz, 10 Hz, 15.6 Hz, and 31.5 Hz. With the damping controller activated, oscillations in the scan images were eliminated, which improved the image quality substantially.

The design of IRC controllers were based on the results presented in Ref. 36 for negative imaginary systems.[37] Of the two independent SISO IRC designs considered one of them, $G_+(s)$, was negative imaginary, while the other, $G_-(s)$, was approximated to be a negative imaginary system. In Ref. 38, results on negative imaginary systems have been extended to systems that are partly negative imaginary. Therein, it has been shown that if the controller $C(s)$ is negative imaginary, and the plant $G(s)$ violates the negative imaginary condition in certain frequency intervals, say $[\omega_k, \omega_{k+1}]$, for $k = 1, 2, \ldots$, then the closed loop is stable if

1. $G(\infty)C(\infty) = 0$,
2. There exists constants K_1 and K_2 such that $|G(0)| < K_1$, $|C(0)| < K_2$ and $K_1K_2 < 1$,
3. In the intervals $[\omega_k, \omega_{k+1}]$, for $k = 1, 2, \ldots$ where $G(\mathrm{i}\omega)$ is not negative imaginary both $G(\mathrm{i}\omega)$ and $C(\mathrm{i}\omega)$ must be bounded, i.e., $|G(\mathrm{i}\omega)| < K_1$ and $|C(\mathrm{i}\omega)| < K_2$ for all $\omega \in [\omega_k, \omega_{k+1}]$, for $k = 1, 2, \ldots$.

However, the above mentioned sufficiency conditions are too conservative. It can be checked that they do not hold in the case of $G_-(s)$. From a theoretical perspective, a tighter sufficiency condition would be worth looking into.

ACKNOWLEDGMENT

This research was supported by the Australian Research Council. The research, including all the experiments were performed in the Laboratory for Dynamics and Control of Nanosystems at the University of Newcastle.

[1] G. Binning, C. F. Quate, and C. Gerber, Phys. Rev. Lett. **56**, 930 (1986).
[2] T. Ando, Nanotechnology **23**, 062001 (2012).
[3] M. J. Rost, L. Crama, P. Schakel, E. van Tol, G. B. E. M. van Velzen-Williams, C. F. Overgauw, H. ter Horst, H. Dekker, B. Okhuijsen, M. Seynen *et al.*, Rev. Sci. Instrum. **76**, 053710 (2005).
[4] T. Ando, T. Uchihashi, N. Kodera, D. Yamamoto, M. Taniguchi, A. Miyagi, and H. Yamashita, J. Mol. Recognit. **20**, 448 (2007).
[5] G. Schitter, R. W. Stark, and A. Stemmer, Ultramicroscopy **100**, 253 (2004).
[6] W. Gao, R. J. Hocken, J. A. Patten, and J. Lovingood, CIRP Ann. **49**, 439 (2000).
[7] B. W. Ahn and S. H. Lee, J. Micromech. Microeng. **19**, 045028 (2009).
[8] Y. J. Chen and J. H. Hsu, Nanotechnology **16**, 1112 (2005).
[9] D. Croft, D. McAllister, and S. Devasia, ASME J. Manuf. Sci. Eng. **120**, 617 (1998).
[10] D. Wouters and U. S. Schubert, Angew. Chem., Int. Ed. **43**, 2480 (2004).
[11] S. Sundararajan and B. Bhushan, Sens. Actuators, A **101**, 338 (2002).
[12] J. C. Rosa, M. Wendel, H. Lorentz, J. P. Kotthaus, M. Thomas, and K. H, Appl. Phys. Lett. **73**, 2684 (1998).
[13] A. Weckenmann, G. Peggs, and J. Hoffmann, Meas. Sci. Technol. **17**, 504 (2006).
[14] A. D. L. Humphris, B. Zhao, D. Catto, J. P. Howard-Knight, P. Kohli, and J. K. Hobbs, Rev. Sci. Instrum. **82**, 043710 (2011).
[15] P. K. Hansma, G. Schitter, G. E. Fantner, and C. Prater, Science **314**, 601 (2006).
[16] Y. K. Yong, S. Aphale, and S. O. R. Moheimani, IEEE Trans. Nanotechnol. **8**, 46 (2009).
[17] G. M. Clayton, S. Tien, K. K. Leang, Q. Zou, and S. Devasia, J. Dyn. Syst., Meas., Control **131**, 061101 (2009).
[18] A. J. Fleming, A. Wills, and S. O. R. Moheimani, IEEE Trans. Control Syst. Technol. **16**, 1265 (2008).
[19] B. J. Kenton and K. K. Leang, IEEE/ASME Trans. Mechatron. **17**, 356 (2012).
[20] B. Bhikkaji, M. Ratnam, A. J. Fleming, and S. O. R. Moheimani, IEEE Trans. Control Syst. Technol. **15**, 853 (2007).
[21] Y. K. Yong, B. Arain, and S. O. R. Moheimani, Rev. Sci. Instrum. **81**, 033701 (2010).
[22] K. K. Leang and S. Devasia, IEEE Trans. Control Syst. Technol. **15**, 927 (2007).
[23] D. Y. Abramovitch, S. Hoen, and R. Workman, in *Proceedings of the American Control Conference, Seattle, WA, 2008* (IEEE, 2008), pp. 2684–2689.
[24] A. J. Fleming, S. Aphale, and S. O. R. Moheimani, IEEE Trans. Nanotechnol. **9**, 438 (2010).
[25] S. Tien, Q. Zou, and S. Devasia, IEEE Trans. Control Syst. Technol. **13**, 921 (2005).
[26] O. M. E. Rifai and K. Youcef-Toumi, in *Proceedings of the American Control Conference 2001* (IEEE, 2001), Vol. 4, pp. 3251–3255.
[27] Y. Yan, Q. Zou, and Z. Lin, Nanotechnology **20**, 175301 (2009).
[28] F. Marinello, S. Carmignato, A. Voltan, E. Savio, and L. D. Chiffre, J. Manuf. Sci. Eng. **132**, 030903 (2010).
[29] A. Daniele, S. Salapaka, M. V. Salapaka, and M. Daleh, in *Proceedings of the American Control Conference, San Diego, CA, 1999* (IEEE, 1999), pp. 253–257.
[30] G. Schitter, A. Stemmer, and F. Allgower, in *Proceedings of the American Control Conference, 2003* (IEEE, 2003), Vol. 5, pp. 3720–3725.
[31] P. J. Gawthrop, B. Bhikkaji, and S. O. R. Moheimani, Mechatronics **20**, 74 (2010).
[32] Y. K. Yong and S. O. R. Moheimani, IEEE/ASME Trans. Mechatron. **18**, 1060 (2013).
[33] A. J. Fleming and S. O. R. Moheimani, IEEE Trans. Control Syst. Technol. **14**, 33 (2006).
[34] A. Sebastian, M. V. Salapaka, and J. P. Cleveland, in *Proceedings of the 42nd IEEE Conference on Decision and Control, Maui, Hawaii, 2003* (IEEE, 2003), pp. 3343–3344.
[35] I. A. Mahmood and S. O. R. Moheimani, Rev. Sci. Instrum. **80**, 063705 (2009).
[36] S. Aphale, A. J. Fleming, and S. O. R. Moheimani, Smart Mater. Struct. **16**, 439 (2007).
[37] A. Lanzon and I. R. Petersen, IEEE Trans. Autom. Control **53**, 1042 (2008).
[38] S. Patra and A. Lanzon, IEEE Trans. Autom. Control **56**, 1395 (2011).